PLOS ONE

RESEARCH ARTICLE

Rice powder template for hausmannite Mn_3O_4 nanoparticles and its application to aqueous zinc ion battery

Nusrat Tazeen Tonu[1,2], **Parbhej Ahamed**[1], **Mohammad Abu Yousuf**[1]*

1 Department of Chemistry, Khulna University of Engineering & Technology, Khulna, Bangladesh,
2 Chemistry Discipline, Khulna University, Khulna, Bangladesh

* yousuf@chem.kuet.ac.bd

Abstract

In this study, a simple calcination route was adopted to prepare hausmannite Mn_3O_4 nanoparticles using rice powder as soft bio-template. Prepared Mn_3O_4 was characterized by Fourier Transform Infra-Red Spectroscopy (FTIR), Field Emission Scanning Electron Microscopy (FESEM), Energy Dispersive X-ray microanalysis (EDX), Powder X-Ray Diffraction (XRD), Transmission Electron Microscopy (TEM), Brunauer-Emmett-Teller (BET) and Solid state UV-Vis spectroscopic techniques. Mn-O stretching in tetrahedral site was confirmed by FTIR and Raman spectra. % of Mn and O content supported Mn_3O_4 formation. The crystallinity and grain size was found to be 68.76% and 16.43 nm, respectively; tetragonal crystal system was also cleared by XRD. TEM clarified the planes of crystal formed which supported the XRD results and BET demonstrated mesoporous nature of prepared Mn_3O_4 having low pore volume. Low optical band gap of 3.24 eV of prepared Mn_3O_4 nanoparticles indicated semiconductor property and was used as cathode material to fabricate CR-2032 coin cell of Aqueous Rechargeable Zinc Ion Battery (ARZIB). A reversible cyclic voltammogram (CV) showed good zinc ion storage performance. Low cell resistance was confirmed by Electrochemical Impedance Spectroscopy (EIS). The coin cell delivered high specific discharge capacity of 240.75 $mAhg^{-1}$ at 0.1 Ag^{-1} current density. The coulombic efficiency was found to be 99.98%. It also delivered excellent capacity retention 94.45% and 64.81% after 300 and 1000 charge-discharge cycles, respectively. This work offers a facile and cost effective approach for preparing cathode material of ARZIBs.

Citation: Tonu NT, Ahamed P, Yousuf MA (2024) Rice powder template for hausmannite Mn_3O_4 nanoparticles and its application to aqueous zinc ion battery. PLoS ONE 19(6): e0305611. https://doi.org/10.1371/journal.pone.0305611

Editor: Gomaa A. M. Ali, Galala University, EGYPT

Received: March 19, 2024

Accepted: June 3, 2024

Published: June 17, 2024

Data Availability Statement: Data Availability Statement: All relevant data are within the manuscript and its Supporting Information file.

Funding: The author(s) received no specific funding for this work.

Competing interests: The authors have declared that no competing interests exist.

Introduction

Safe, environment friendly, and cost-effective energy storage systems are ideal for large-scale application. Due to increasing urgency of tackling climate change and ecological deterioration, electrochemical energy storage systems are in high demand [1]. Decades have passed since rechargeable lithium-ion batteries dominated energy storage in portable devices and electric vehicles. But, few issues like, safety and eco-friendly stuff, expensive scaling up, and lack of lithium sources are all getting in the way of making big storage for the grid [2]. Lead-acid batteries

(LABs) are the most used rechargeable batteries till now. It comprises about 60% of the world's electric storage batteries [3]. Lead itself is toxic, and after the shelf life the Pb contaminated acid is thrown to the environment in most of the cases. During recycling a significant amount of poisonous Pb and As metals also go in the environment. Moreover, LABs has low energy-efficiency and short lifespan [4]. As opposed to the problems of the above mentioned rechargeable batteries aqueous rechargeable batteries based on Zn^{2+}, Mg^{2+}, Al^{3+}, or Fe^{3+} ions are gaining popularity for low cost, superior conductivity, safety, ease of production, and environmental friendliness. Among them ARZIBs have gained significant consideration to the researchers. ARZIBs use zinc metal anodes, aqueous electrolytes, and different cathodes [5, 6]. Zn anode offers abundant sources, a theoretical high capacity of 820 $mAhg^{-1}$, multivalent charge transport, adequate reduction potential (-0.76 V vs Standard hydrogen electrode), suitable ionic radii of Zn^{2+} ion (0.74 Å), and easy handling. In addition, aqueous electrolytes offer stronger conductivity, less dangers, and more safety. In ARZIBs, Zn anode is fixed but the cathode is different depending on the utilities [7, 8]. Prussian blue analogues (PBAs), manganese, vanadium, and organic species have been used to make ZIB cathodes. PBAs have a high potential (1.6–1.8V) but poor capacity ($<$100 $mAhg^{-1}$) [9]. Although V-based cathode materials delivers high capacity and long cycling rate of performance, but they are costly, poisonous, and have a low voltage of operation (0.6–0.9 V). Likewise, cathode materials having organic framework have high value of specific capacity, but poor conductivity and low operating voltage [10, 11]. On the contrary, Mn-based cathode materials, with polymorphs or different crystal structure (α-, β-, δ-, γ-, λ-, T-type, R-type, ε- MnO_2) and oxidation states (MnO, Mn_2O_3, and Mn_3O_4), have gained the most attention of the researchers for their high specific capacity (308 $mAhg^{-1}$), cost effectiveness, non toxicity, and high operating voltage (1.2–1.5 V) than Zn anodes [12, 13].

As a promising candidate, Mn_3O_4, having chemical formula $Mn(II)Mn(III)_2O_4$, has high capacity and voltage. In real ZIBs, these manganese oxides always have low conductivity and high volume expansion during cycling, causing electrode pulverization, structural collapse, and quick capacity fading. To obtain high-rate and long-life ZIBs, Mn_3O_4 needs innovative design methodologies [14, 15]. Spinel structured Mn_3O_4 is known for its thermodynamic stability, which helps prevent structural collapse during the electrode reaction process as well as impressive charging-discharging cycling stability and good capacity retention [16]. The distinctive and unwavering hausmannite structure exhibited by Mn_3O_4 at ambient temperature facilitates the production process of phase-pure Mn_3O_4 nanocrystals. These factors provide significant advantages to Mn_3O_4 as electrode materials for energy storage. Nevertheless, the practical implementation of Mn_3O_4 is constrained by its low active surface area, contemptable electronic conductivity, and vulnerability of accumulation during the synthesis route [17]. These disadvantages of Mn_3O_4 also limit its practical application in electrochemical energy storage systems. Several methods have been adopted to improve its electrochemical performance, such as- particle size reduction, uniform distribution of particles, and/or creating a mesoporous structure [18, 19]. Zhang *et al*. have effectively synthesized a diverse array of Mn_3O_4 nanorods featuring various nanostructures and microstructures. At applied current density of 0.1 Ag^{-1}, the Mn_3O_4 electrode showed a specific capacitance of 136.5 Fg^{-1} [20]. In 1.0 M Na_2SO_4, Liu *et al*. synthesized solid nano-spheres of Mn_3O_4 which showed a specific capacitance of 150 Fg^{-1} at 0.3 Ag^{-1} current density [21]. In order to fabricate the $Co(OH)_2$/Mn_3O_4 nanocomposites, Liu *et al*. utilized a facile ion diffusion technique to inject Co ions into Mn_3O_4. This modification significantly enhanced the aggregation characteristics of the Mn_3O_4 nanoparticles, as well as their conductivity and specific capacitance [22].

The method of using template for producing nanomaterials offers synthetic materials with controllable morphology, structure, and size with a high repetition rate. Rice powder being a

non-metallic soft template is suitable for metal oxide nanoparticle synthesis [23]. In rice, starch is the main component. Starch consists carbohydrate polymeric chains which are build up from small glucose molecules and are parted in amylase (linear) and amylopectin (branched) units. These specific distinct characteristics of rice are the basic foundations for the synthesis of nanomaterials of different sizes and shapes [24]. Therefore, using rice powder as a sift bio template seem to be a promising way to synthesize manganese based oxide nanoparticles.

Lots of experiments have been done for the synthesis of various functional materials by using rice husk [23, 25] and starches [26, 27]. However, to the best of our knowledge, no such study has been found in the open literature for the synthesis of Mn_3O_4 nanoparticles using rice powder as soft bio template. Keeping in mind, in our study, rice powder was chosen as a soft template for the preparation of Mn_3O_4 nanoparticles due to the reasons- (i) its high porous structure, (ii) spongy character with water, (iii) special components having thermal degradation property, (iv) cost effective, and (v) available in local market. We hope this study will contribute some knowledge worth to be carried out. The prepared Mn_3O_4 has been characterized by FTIR, Raman, FE-SEM, EDX, TEM, BET, solid state UV- Visible spectroscopy and powder XRD techniques. Results showed nano sized Mn_3O_4 particle having low band gap and that was used as cathode material to fabricate CR-2032 coil cell of ARZIBs. Then the fabricated CR-2032 coil cell has been tested by CV, Battery Charging-Discharging (BCD) profile and EIS techniques to assess its electrochemical performance for reversible zinc ion storage.

Materials and methods

Chemicals and instruments

Manganese (II) acetate tetrahydrate, $(CH_3COO)_2Mn.4H_2O$, was purchased from Sigma-Aldrich (USA). Rice powder was purchased from local stationary shop (Bangladesh). Stainless steel (SS) substrates (304 grades) of thickness t-0.01× w-100mm, Zinc foil, polyvinylidene fluoride (PVDF), n-methyl pyrrolidone (NMP), carbon black (C-black) were used for the preparation of the CR-2032 coin cell battery. The whole experimental was carried out using deionized (DI) water.

The structure and morphology of prepared Mn_3O_4 was investigated using FE-SEM machine (JSM-7610F, Japan). XRD analysis was done using X-ray diffractometer (XRD; Bruker, D2 PSA-SER) with Cu Kα radiation at 2θ from 10˚ to 80˚. TEM analysis was done by JEOL TEM (Model: JEM 2100 PLUS, JEOL, Japan). Few amount of prepared sample was taken in a test tube containing ethanol and was shaken well. It was covered by a cork and sonicated for 30 min. Then the tube was kept at rest for a day. A drop of the sonicated sample was taken in a copper grid and kept in a vacuum chamber overnight for degassing. Then the copper grid contain sample was tested by TEM analyzer. BET was carried out using BET Sorptometer (Model: BET-201-A, ID: CRF-FR.B.02, PMI, USA). The prepared sample was pretreated with degassing at 90˚C for 3 h followed by 20 microns vacuum at 130˚C overnight in an oven with high purity nitrogen purge. Then it was analyzed by BET analyzer with respect to the adsorption/desorption of nitrogen. The thermal stability of rice powder was investigated using TGA machine (TGA-50, Shimadzu, Japan), from room temperature to 800˚C (10˚C/min, 2mL/min Air, Pt pan). To examine the semiconductor behavior of prepared Mn_3O_4, solid state UV-visible spectroscopic test was carried out within the range 300–800 nm using UV-1800 spectrophotometer of Shimadzu Corporation, Japan. CV, EIS and BCD were performed via Biologic (SP-300) potentiostat.

Preparation of Mn_3O_4 using rice powder as template

20 mL of deionized water was taken in a crucible. 1.0 g of manganese (II) acetate tetrahydrate was added in it and stirred until a homogeneous solution is formed. Then 2.0 g of rice powder

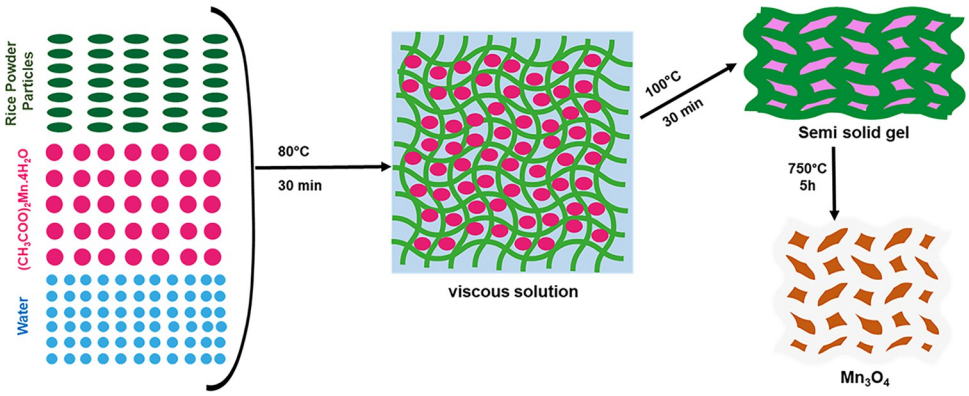

Fig 1. Schematic diagram for the synthesis of Mn_3O_4.

https://doi.org/10.1371/journal.pone.0305611.g001

was added in the mixture. The weight ratio of manganese (II) acetate tetrahydrate and rice powder is 1:2. Rice powder began to absorb the mixture and got swell. Then it was heated at 80˚C. Rice powder began absorb manganese (II) acetate tetrahydrate and water and form a thick white viscous solution. The solution was heated with continuous stirring for 30 min until it got more viscous (semi-solid gel) in appearance. Then it was heated at 110˚C for 30 min. After that the crucible containing the mixture was calcined at 750˚C for 5h and allowed to cool ad room temperature. Meanwhile the manganese (II) acetate tetrahydrate content in the mixture endure a chemical reaction and form Mn_3O_4 and left a dark brown colored solid foam of Mn_3O_4. Fig 1. Shows the schematic diagram for the synthesis steps of Mn_3O_4. Then it was grinded in a manual mortar/pastel and used for further experiments [28]. The formation of Mn_3O_4 nanoparticles could be suggested by following mechanism [29].

$$Mn(C_7H_6O_2)_n \overset{750^{\circ}C}{\rightarrow} CO_2 + H_2O + MnO;\ \text{n} = 1 \text{ or } 2$$

$$2MnO + \frac{1}{2}O_2 \rightarrow Mn_2O_3$$

$$Mn_2O_3 + MnO \rightarrow Mn_3O_4$$

Coin cell fabrication

After Mn_3O_4 was prepared, it was mixed with C-black, PVDF (8:1:1) and NMP as solvent. It was pasted by a mortar/pastel to make paste. Then it was applied on a SS foil to form a thin film on it. Then it was dried at 70˚C until it hardened and then cut in to desired shape by battery dice cutting machine to have the final cathode part of CR-2032 coil cell. The pasting and casting of cathode material was manually done. That's why every battery has different amount of cathode material as well as active material having constant ratio of Mn_3O_4, C-black and PVDF was 8:1:1. The amount of active material was calculated after cutting the cathode followed by weighing manually. The battery used for CV and BCD tests had cathode material of 0.02 and 0.008 g respectively. To fabricate a CR-2032 coil cell, the metal cases, cathode, separator, anode, spacer and spring were arranged. Then it was pressed by crimping machine to have the desire final CR-2032 coin cell. The separator was soaked with electrolyte (Aqueous solution of 2.0 M of Zinc sulphate heptahydrate ($ZnSO_4.7H_2O$). About 10 batteries were fabricated and used for electrochemical assessments [30].

Results and discussion

Prepared Mn-oxide was analyzed by FTIR spectroscopy (range 450–4000 cm^{-1}). The spectrum Fig 2(A) of the prepared Mn-oxide displayed two significant peaks within the range of 450–650 cm^{-1}. The peak located at 633 cm^{-1} represents Mn-O stretching vibration in tetrahedral sites, whereas, the peak located at 524 cm^{-1} denotes the distortion vibration of Mn-O in an octahedral site. The weak band at 1049 cm^{-1} could be count for υMn–O–H vibration. This result indicated that the prepared compound was Mn-oxide [31, 32]. FTIR spectrum also consistent with reported references of [33] Mn_3O_4 prepared by one step synthesis from Manganese acetate tetrahydrate and N, N-Dimethyl formamide.

The thermal property of rice powder provides the evidence on the physical properties of the components present in it. As a complex mixture, rice powder, consists starch, non-starch, lipids, polysaccharides, sugars, proteins, minerals and fibers at high content [34]. Fig 2(B) shows the TGA of rice powder. The results indicated that, rice powder started to loss its weight at 40.85˚C and it loosed 98.59% of its mass at a temperature bellow 100˚C, the weight loss was for the moisture content present in it. (A) 40.85˚C to 241.31˚C associated with water loss; (B) 241.31˚C to 322.11˚C related with the decomposition of starch, non-starch polysaccharides, sugars, proteins and small amount of lipids.; and (C) 322.11˚C to 607.57˚C regarding the decomposition of fibers and long chain lipid fragments present in it. After 650˚C, about 1.4% weight of rice powder was present which is expected to be carbon [34]. For template assisted synthesis of inorganic nanoparticles, it is necessary to eliminate the template after nanoparticle production to have the pure form of nanoparticles as much as possible. Thus, template could participate in nanoparticle production but could not get itself involve in the application of that nanoparticles. So, as a template at temperature 750˚C, rice powder is a very good choice [35].

To examine the surface morphology FESEM micrographs were analyzed [Fig 3(A) and 3 (B)]. The grains of prepared Mn-oxide were of uneven shapes and sizes. The surfaces were seem to be porous as well. In the calcination process for template elimination at 750˚C, the removal of rice powder leads to the existence of pores in Mn_3O_4 samples, however these pores are also of irregular sizes. These pores reinforce the electrochemical activity which in this case in favor of energy storage application. Employing ImageJ software, the average particle size was computed by histogram [Fig 3(C)], and it was found to be 53.67 nm [36, 37].

EDX technique was used to assess the composition and stoichiometry of prepared Mn-oxide. Fig 3(D) shows the EDX spectrum of prepared Mn_3O_4 samples. Peaks in EDX spectra indicates the presence of Mn and O elements with very little amount of impurity. The EDX lines observed at 5.905 and 0.532 keV are associated for K lines of the Mn and O elements,

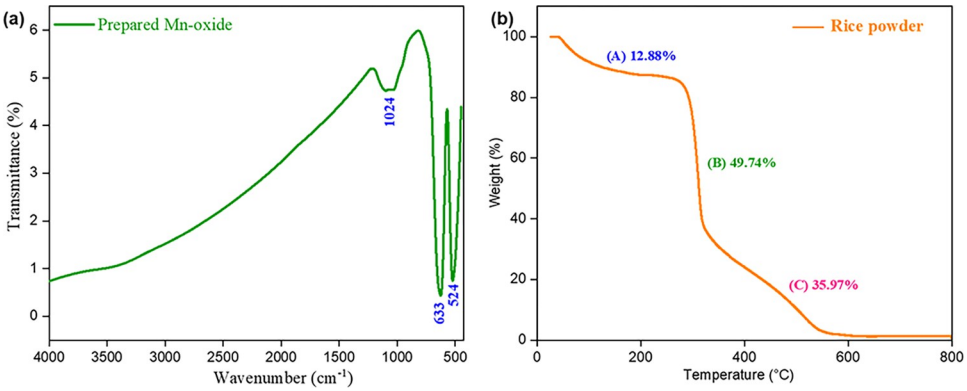

Fig 2. (a) FTIR spectrum of Prepared Mn_3O_4 nanoparticle, (b) TGA of rice powder.

https://doi.org/10.1371/journal.pone.0305611.g002

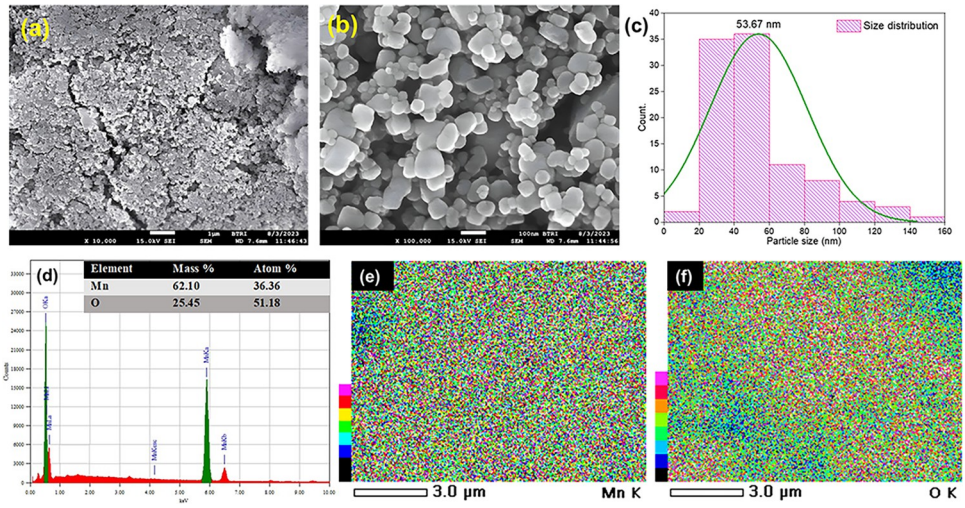

Fig 3. (a and b) FESEM image of prepared Mn_3O_4 particles of scaling 1μm and 100 nm respectively, (c) histogram of the particle size distribution of prepared Mn_3O_4, (d) EDX spectra of Mn_3O_4 particles (inset shows the percentage of major elements), and (e and f) Elemental mapping of Mn and O.

https://doi.org/10.1371/journal.pone.0305611.g003

respectively. The elemental mapping [Fig 3(E) and 3(F)] depicts the elements Mn and O are uniformly distributed over entire Mn-oxide samples. Accordingly, the composition of Mn and O in the prepared sample was 36.36% and 51.18%, respectively, by mass. This indicates the ratio of Mn:O is very close to 3:4. Therefore, from EDX result, it was confirmed that the prepared sample was Mn_3O_4 [32].

The prepared Mn-oxide powder was examined by Powder X-ray Diffractometer to identify its phase and crystal structure. Fig 4(A) shows the powder XRD spectrum of prepared Mn-oxide which was happened to be Mn_3O_4 nanoparticles. The production of Mn_3O_4 was confirmed by the diffraction peaks at 2θ = 18.21˚, 28.91˚, 31.04˚, 32.35˚, 36.12˚, 36.51˚, 38.02˚, 44.30˚, 49.86˚, 50.74˚, 53.90˚, 56.04˚, 58.56˚, 59.89˚, 63.14˚, 64.68˚, 67.70, 69.72˚, 74.18˚, 76.60˚ and 77.55˚; were assigned to the planes (011), (112), (020), (013), (121), (022), (004), (220), (024), (015), (132), (033), (231), (224), (166), (040), (026), (035), (143), (242) and (044), respectively; which were well matched with Crystallographic Open Database (COD) entry #1514240 (pdf # 96-151-4241) [38]. This can be attributed to the tetragonal crystal system of I

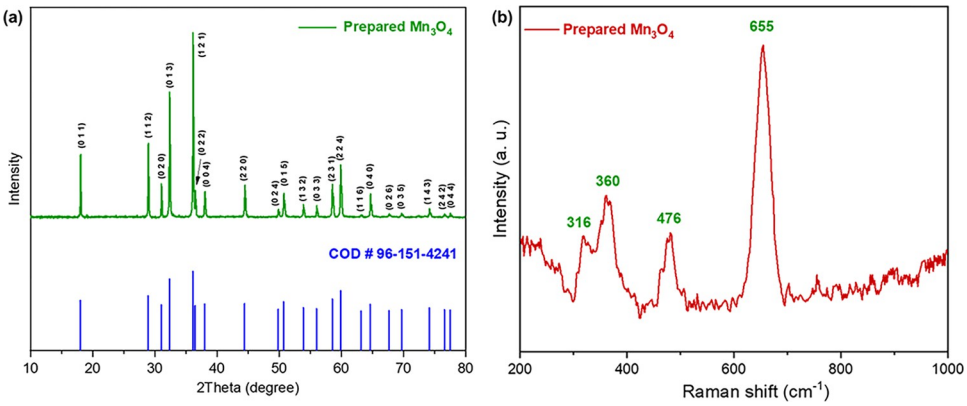

Fig 4. (a) Powder XRD pattern and (b) Raman spectra of the prepared Mn_3O_4 nanoparticles.

https://doi.org/10.1371/journal.pone.0305611.g004

41/a m d (141) space group having hausmannite phase of Mn_3O_4 nanostructure. No extra peaks were found in XRD pattern for impurities. This denotes the purity of prepared Mn_3O_4 powder. This XRD spectrum was well matched with that of Mn_3O_4 nanoparticles synthesized by co-precipitation method using manganese chloride and manganese acetate as precursor [39].

The average crystal size was calculated using Scherer equation [40],

$$d = \frac{K\lambda}{\beta Cos\theta} \quad \text{(i)}$$

where, D = crystallite size in nm, K = Scherer constant, λ = wavelength of X-ray in nm, β = full wave half maximum (FWHM) of the XRD peaks and θ is Braggs angle. An average crystallite size of 16.43 nm was observed. The crystallinity was found to be 68.76% [32].

Bragg's law [40] was used to calculate the d-spacing-

$$n\lambda = 2dsin\theta,$$

,

$$\text{or, } d = \frac{n\lambda}{2sin\theta} \quad \text{(ii)}$$

Where, λ = 1.5406 Å (wavelength of incident X-ray), θ = Peak position (in radians), n = 1 (order of diffraction), d = interplaner spacing or d-spacing (in Å)

The equation of lattice constant for a tetragonal unit cell was calculated using equation [41],

$$\frac{1}{d^2} = \frac{h^2 + k^2}{a^2} + \frac{l^2}{c^2} \quad \text{(iii)}$$

Where, h, k, and l is the miller indices; d indicates interplanar spacing; a and c indicates the lattice constants of unit cell. Using the value of the planes (0 0 4) and (0 2 0) at 2θ = 38.02˚ and 31.04˚, respectively, the lattice parameters were calculated [42]. The values calculated from Eq (ii) and (ii) are given bellow in Table 1. The calculated values of lattice parameter a = b = 5.757644 Å and c = 9. 459276 Å. These values are in very good approximation to the standard values [38].

Raman spectra of prepared Mn_3O_4 is shown in Fig 4(B). Four peaks were observed; one strong peak at 655 cm^{-1} and three small broad peaks at 316, 360 and 476 cm^{-1}. These peaks indicated the skeletal vibration of Mn_3O_4. The strongest and sharp peak at 655 cm^{-1} could be assigned to A_{1g} mode, which supported the Mn-O breathing vibration of divalent Mn ions in tetrahedral coordination. This result was in good agreement with the mineral hausmannite, as in both chemically prepared samples and commercial powders [43, 44].

To verify the results of FESEM and XRD, TEM experiment was performed. Fig 5 shows the TEM micrographs of prepared Mn_3O_4 nanoparticles. The particles are of irregular shapes and sizes [Fig 5(A), 5(E) and 5(J)]. The average particle size distribution is around 12.10 nm confirmed by histogram [Fig 5(B)]. Highly oriented crystal planes are noticed from Fig 5(C), 5(E) and 5(J) revealing good crystallinity of the Mn_3O_4 nanoparticles. ImageJ software was used to find out the d-spacing (0.12, 0.31, 0.21, 0.18 and 0.27 nm) for corresponding planes [(044), (112), (220), (024) and (013)] by creating line intensity graphs [Fig 5(D), 5(G), 5(I), 5(L) and 5(N)] of selected areas [Fig 5(C), 5(F), 5(H), 5(K) and 5(M)]. This values are well matched with Crystallographic Open Database (COD) entry #1514240 (pdf # 96-151-4241) [38].

Table 1. Values of peak position, interplanar spacing, miller indices and lattice constants from XRD pattern.

No.	Peak position 2Theta (˚)	Interplanar spacing d (Å)	Miller indices (h k l)	Lattice constant			
				a = b		c	
				Standard (Å)	Calculated (Å)	Standard (Å)	Calculated (Å)
1.	18.21	4.867792	0 1 1	5.76	**5.757644**	9.46	**9.459276**
2.	28.91	3.085896	1 1 2				
3.	31.04	2.878822	0 2 0				
4.	32.35	2.765173	0 1 3				
5.	36.12	2.484736	1 2 1				
6.	36.51	2.459084	0 2 2				
7.	38.02	2.364819	0 0 4				
8.	44.30	2.043059	2 2 0				
9.	49.86	1.827474	0 2 4				
10.	50.74	1.797825	0 1 5				
11.	53.90	1.699643	1 3 2				
12.	56.04	1.639705	0 3 3				
13.	58.56	1.575004	2 3 1				
14.	59.89	1.543166	2 2 4				
15.	63.14	1.471330	1 1 6				
16.	64.68	1.439968	0 4 0				
17.	67.70	1.382893	0 2 6				
18.	69.72	1.347684	0 3 5				
19.	74.18	1.277300	1 4 3				
20.	76.60	1.242862	2 4 2				
21.	77.55	1.229993	0 4 4				

https://doi.org/10.1371/journal.pone.0305611.t001

To analyze the surface properties of prepared Mn_3O_4 nanoparticle, BET experiment was carried out. The specific surface area was calculated using classical BET equation [45]-

$$\frac{P}{V(P_{0-P})} = \frac{1}{V_m c}x + \left(\frac{c-1}{V_m C}\right)\frac{P}{P_0} \quad \text{(iv)}$$

Where, V is the volume of adsorbed molecules, V_m is the monolayer volume, c is the BET constant related to the adsorbate-adsorbent interaction strength and the heat of adsorption, and P/P_0 is the relative pressure. The higher value of c, the higher the interaction [46]. Fig 6(A) shows N_2 adsorption-desorption isotherm of prepared Mn_3O_4 nanoparticle. Fig 6(B) shows Brunauer-Emmett-Teller (BET) plot for specific surface area calculation. Here, slope is 0.195866, y-intercept is 0.054145, correlation coefficient, R^2 is 0.993373. The calculated value of V_m is 3.999831 and C is 4.617448. The BET specific surface area (SSA) can be calculated using following equation [45]:

$$SSA = \frac{V_m N_A a_m}{V m_s} \quad \text{(v)}$$

Where, N_A is the Avogadro's number (6.022×10^{23} mol^{-1}), a_m is the effective cross-section area of one adsorbed molecule of N_2 (0.162 nm^2), V is the molar volume of one adsorbed molecule (22.414 L), and m_s is the mass of adsorbent. The calculated value of SSA is 17.431304 m^2/g.

The pore size distribution of prepared Mn_3O_4 nanoparticle was determined using Barrett-Joyner-Halenda (BJH) method from adsorption-desorption branch of the isotherm [Fig 6(C)]. Given porosity based on skeletal density of 1.0 g/cc = 0.0202 per gram of sample, the calculated

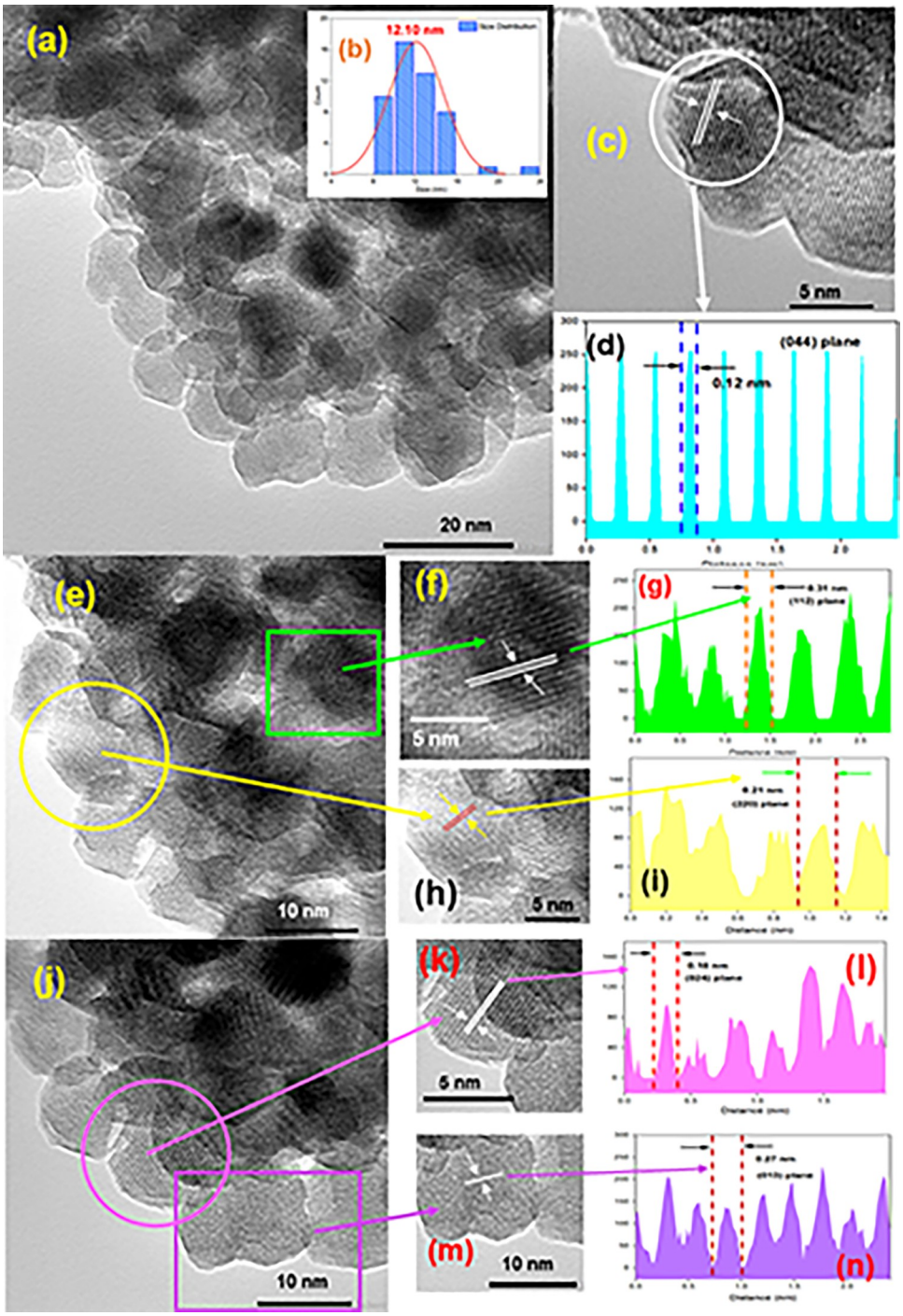

Fig 5. TEM micrographs of prepared Mn_3O_4 nanoparticles at scaling (a) 20 nm, (c) 5 nm, (e) & (j) 10 nm; (f) & (h) and (k) & (m) are cross sections of (e) and (j) respectively (inside showing scaling); (d) histogram for particle size distribution of (a); (d), (g), (i), (l) and (n) are corresponding line intensity profile of (c), (f), (h), (k) and (m).

https://doi.org/10.1371/journal.pone.0305611.g005

values of average pore diameter and total pore volume is 47.2727 Å and 0.0206 cc/g for both adsorption and desorption studies [47, 48]. This study indicates prepared Mn_3O_4 nanoparticle is mesoporous material and is well matched with previously reported results for pure Mn_3O_4 nanoparticle [49].

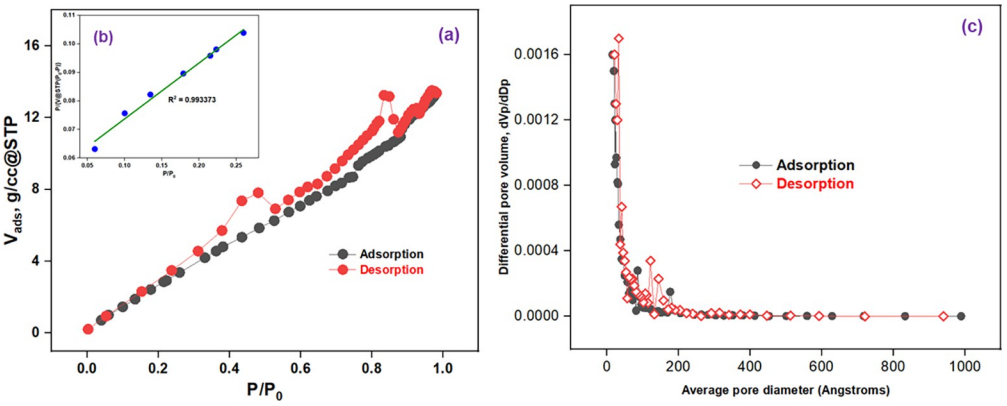

Fig 6. (a) Nitrogen adsorption-desorption isotherm of prepared Mn_3O_4 nanoparticle, (b) BET plot, and (c) BJH pore size distribution curves.

https://doi.org/10.1371/journal.pone.0305611.g006

The absorption spectra for the prepared Mn_3O_4 nanoparticles is shown in Fig 7(A). The absorption coefficient (α) was calculated from the following equation [50] of optical absorption spectra-

$$\propto = \frac{A}{d} \tag{vi}$$

Where, d is the thickness of the specimen. The photon dependency of the absorption coefficient can be described by Tauc's equation [51] given bellow-

$$(\propto hv)^2 = B(hv - E_g) \tag{vii}$$

Where, B is the parameter that depends on the transition probability and Eg is the optical energy gap. Fig 7(B) shows the absorption coefficient in the form of $(\alpha h\nu)^2$ versus hν for the prepared Mn_3O_4 nanoparticles. The intercepts of the straight lines with the photon energy axis gives the optical band gap, which was found to be 3.24 eV, represents the semiconductor property of prepared Mn_3O_4 nanoparticles. This value is comparably higher than the samples found in the literature [52, 53]. From the part of XRD and TEM, we can see that sample had

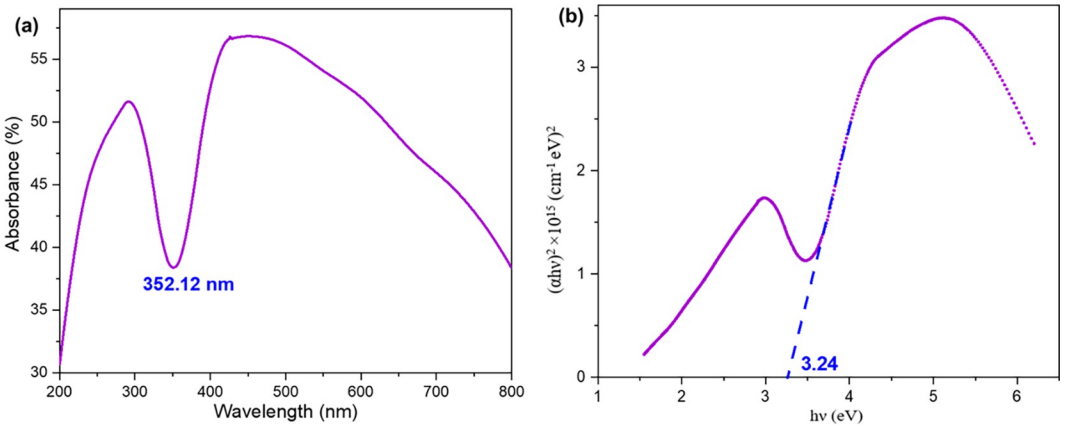

Fig 7. (a) Absorption spectra, (b) Absorption coefficient in the form of $(\alpha h\nu)^2$ versus hν for the prepared Mn_3O_4 nanoparticles.

https://doi.org/10.1371/journal.pone.0305611.g007

small crystallite size of highly oriented crystal planes with good crystallinity. In case of metal oxides, sometimes band gap (E_g) value increases because of the cracking between unit cells when the size of the particle is smaller. This wider band gap of prepared Mn_3O_4 nanoparticles occurred because of the quantum confinement effect due to its smaller size of crystallite [29].

CV was performed for the prepared CR-2032 coin cell within electrochemical window +0.8 V to +2.0 V at different scan rates, 0.1, 0.2, 0.3, 0.4 and 0.5 mV/s. one well resolved anodic peak at +1.51V to+1.58 V and two cathodic peaks were appeared at +1.38 to +1.33 V and +1.21 to +1.17 V [Fig 8(A)] and have similar oxidation and reduction peaks in each CV with different scan rates. In anodic process, one sharp oxidation peak at +1.58 V can be attributed to the intercalation of Zn^{2+} ion into the interlayer of hausmannite structure. This indicates the transition of cathode material from Mn_3O_4 to Mn_5O_8 for Zn^{2+} ion storage purpose. The electrochemical behavior corresponding to the two reduction peaks are the deintercalation of Zn^{2+} into the interlayer of hausmannite structure and H^+ extraction with the reduction of Mn(II) to Mn(III), respectively. This confirms the process of H^+ and Zn^{2+} co-deintercalation. With increasing of scan rates the peak heights of peak1, peak2 and peak3, as labelled in Fig 8(A), increased. High scan rate increases the reaction rate thereby quickens the electron transfer process [10]. From this result, probable reaction could be given as-

$$Anode\ reaction:\ Zn \leftrightarrow Zn^{2+} + 2e^{-}$$

$$Cathode\ reaction:\ 2Mn_3O_4 + 2e^{-} \leftrightarrow Mn_5O_8 + Mn^{2+}$$

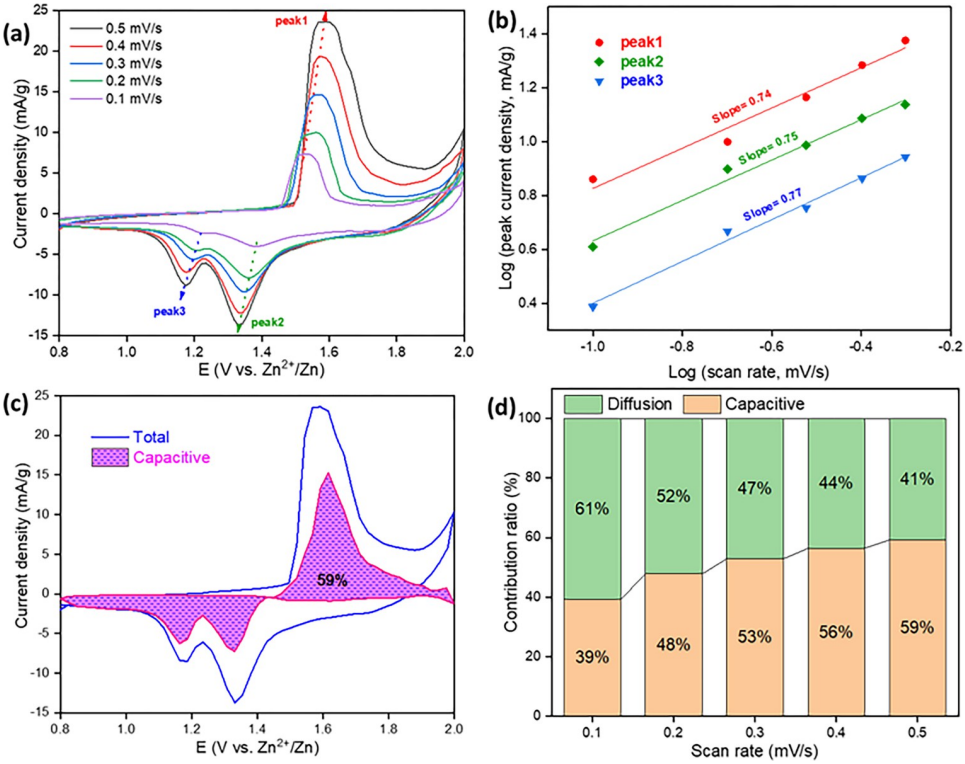

Fig 8. (a) CV curves pf fabricated coin cell at different scan rates, (b) the fitted lines: Log(peak current density) vs Log (scan rate), (c) capacitive contribution to the total capacity at scan rate 0.5 mV/s, and (d) capacitive and diffusion contribution to the total capacity at different scan rates.

https://doi.org/10.1371/journal.pone.0305611.g008

$$H_2O \leftrightarrow H^+ + OH^-$$

Similar result has been found for Mn_3O_4 nanoflower based composite cathode for ARZIB [54]. The behavior of the CV was tested by Dunn's method [55]:

$$Log\ i = Log\ a + b\ Log\ v \quad \text{(viii)}$$

Where, a and b are constants. The value of b was obtained between 0.5 and 1.0. If the value of the slope (b) is 0.5, it denotes a diffusion- controlled behavior (Q_d) and if it is 1.0, it implies capacitive process (Q_c). A graph was plotted as *Log v* (scan rate) vs *Log i* (peak current density) and the value of slope (b) for anodic (peak1) is 0.74 and cathodic (peak2 and peak3) is 0.75 and 0.77, respectively. From the graph [Fig 8(B)], the result is b = 0.74, 0.75 and 0.77; which is below between 0.5 and 1.0; indicates the total electrochemical storage mechanism includes diffusion controlled pseudo capacitive behavior of a battery characteristics [56, 57]. The storage mechanism of Zn^{2+} has excellent non-diffusion limits because of Mn_3O_4 nanoparticles. The capacitive contribution ratio was calculated on the basis of anodic behavior of the cell using the following equation [56]:

$$i_p(v) = k_1 v + k_2 v^{\frac{1}{2}}$$

$$\text{Or,} \qquad \frac{i_p}{v^{\frac{1}{2}}} = k_1 v^{\frac{1}{2}} + k_2 \quad \text{(ix)}$$

Where, k_1 and k_2 are the slope and intercept of $v^{\frac{1}{2}}$ vs $\frac{i_p}{v^{\frac{1}{2}}}$ plot [S1 Fig in S1 File]. The pseudo-charge storage contribution is $k_1 v$, and the insertion type capacity is $k_2 v^{1/2}$ [58, 59]. As compared with the total charge storage contribution, the capacitive contribution was around 59% at 0.5 mV/s scan rate, indicated the process was capacitive dominated [Fig 8(C)]. With the increasing of the scan rates 0.1, 0.2, 0.3, 0.4, and 0.5 mV/s, the capacitive contribution was 39%, 48%, 53%, 56%, and 59%, respectively. The results from Fig 8(D) showed that the capacitive contribution gradually increased with the scan rates and finally reached a maximum value of 59% at 0.5 mV/s. this indicated the enhanced pseudo-capacitive behavior of nanoparticle morphology [60]. In a word, it can be said that the total process was controlled by capacitance at high current densities. These values of b (slope1, 2 and 3) [Fig 8(B)] of CV peaks had very close values as compared to the values with Mn_3O_4@C hierarchial nanospheres. Besides the capacitivie contributions are also comparable [10].

Fig 9(A) represents the battery charge-discharge (BCD) curve of fabricated coin cell having Mn_3O_4 as cathode at different current density. It shows with the increasing of current density (0.1, 0.2, 0.3, 0.4, 0.5 and 0.6 A/g) the specific discharge capacity decreases (240.75, 196.15, 168.62, 154.48, 115.04 and 60.71 mAh/g, respectively). Rate capability was also tested at those current densities [Fig 9(B)]. When current density drops back to the initial 0.1 Ag^{-1}, the specific discharge capacity was found to be 234.44 $mAhg^{-1}$, which is almost recovered from its initial value 240.75 mAh/g, corresponding to about 97.37% retention. It is seen that the discharge capacity is a litter lower than the charging capacity. This is because after every charging a very small amount of Zn^{2+} may got trapped in the cathode materials or form stable complexes with it, which blocked the available intercalation sites. The coulombic efficiency was found to be 99.98%. BCD cycling performance [Fig 9(C)] was also done at 0.1 A/g current density over 1000 cycles. After 100, 200, 300, 400, 500, 600, 700, 800, 900 and 1000 cycles the specific discharge capacity retention was found to be 97.19%, 96.34%, 94.45%, 91.78%, 89.21%, 84.09%,

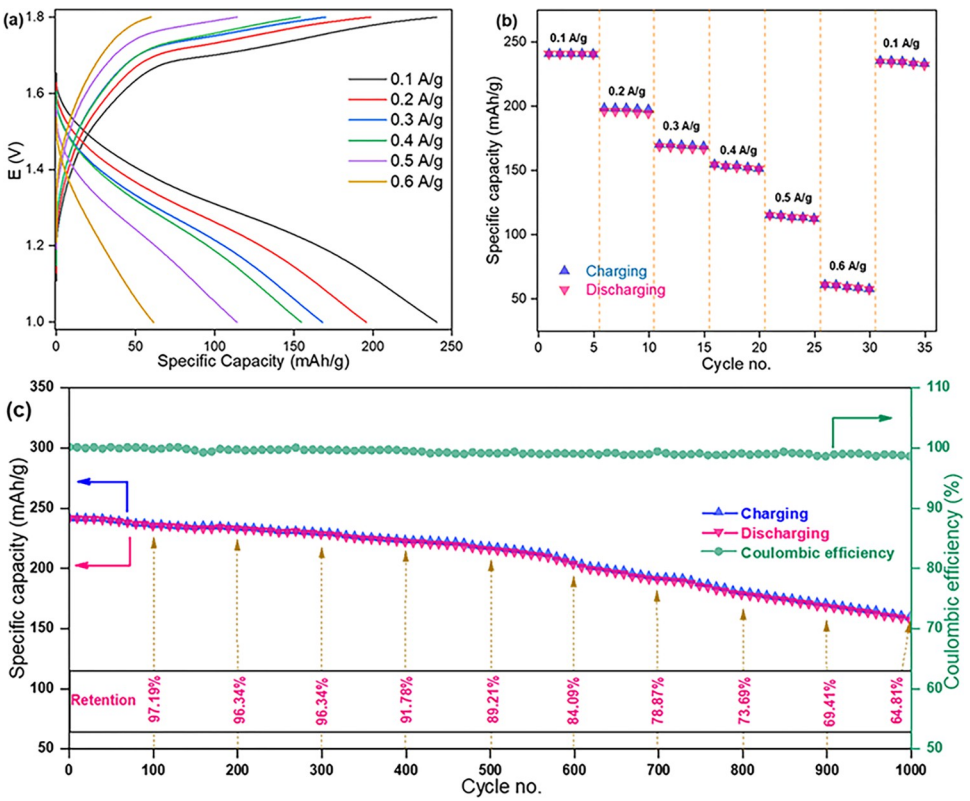

Fig 9. BCD profile of fabricated coin cell (a) Specific capacity at different current density, (b) rate capability at different current density, (c) cycling performance, coulombic efficiency and specific discharge capacity retention at 0.1 A/g over 1000 cycles.

https://doi.org/10.1371/journal.pone.0305611.g009

78.87%, 73.69%, 69.41% and 64.81%, respectively [61, 62]. These values of specific discharge capacities with retention was very close to the previously reported results of Mn_3O_4 applied in ARZIBs [17].

Fig 10 shows the electrochemical impedance profile of fabricated CR-2032 coin cell. The experiment was carried out at potential +1.9 V at 300 kHz to 100 mHz frequency region. This applied potential is a little bit higher than the oxidation potential of the coin cell. The equivalent circuit R1+Q2/R2+Q3/R3+W4 was used to evaluate the Nyquist plot [Fig 10(A)]. Here, R1 represents solution resistance in ohm, R2 represents electrode resistance due to solution electrolyte interface (SEI) contribution in ohm, R3 represents charge transfer resistance in ohm, Q2 and Q3 represents constant phase elements (CPE), which had been usually used for porous materials and W4 represents Warburg impedance in ohm.$s^{1/2}$ [63, 64]. The coin cell showed the values of R1, R2, R3 and W4 were 6.78 Ω, 14.88 Ω, 27.75 Ω and 6.99 Ω$s^{1/2}$ for before BCD; and 7.257 Ω, 32.15 Ω, 38.28 Ω and 16.92 Ω$s^{1/2}$ for after BCD of 1000 cycles, respectively. The resistances are lower for fresh battery but higher after BCD cycling. The equivalent circuit fits at higher frequency and slightly deviates as the frequency decreases. This could be explained in terms of the formation of secondary capacitors with in the coin cell. Furthermore, the coin cell fabrication process was manual; the pasting and casting of cathode material on cathode current collector foil; and the separator was ordinary filter paper. While crimping the cell by crimping machine at high pressure, it may be possible that some of the cathode went into the filter paper. BCD testing took long time also, some cathode materials from the cathode current collector might got detached, traveled through the separator filter

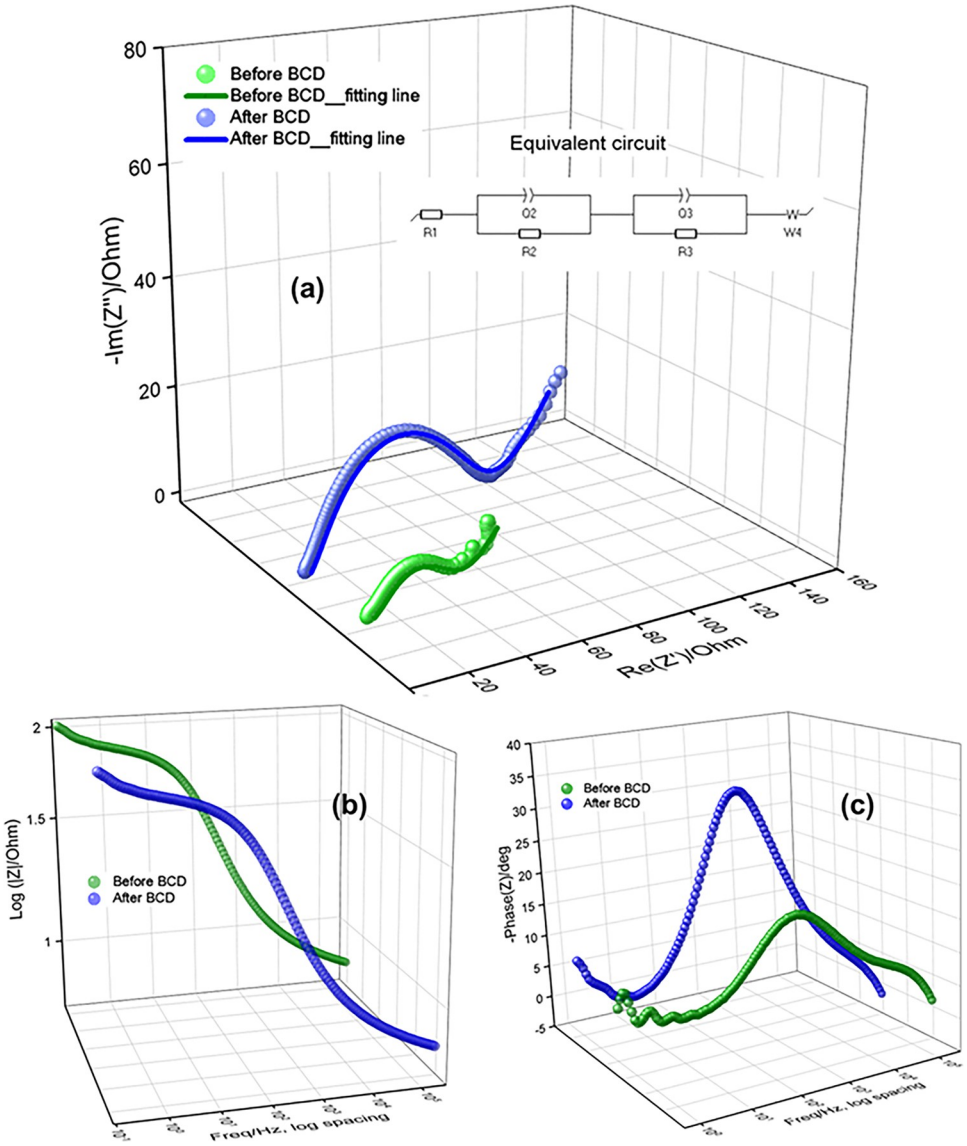

Fig 10. EIS of fabricated CR-2032 coil cell (a) Nyquist plot (inside shows equivalent circuit). Bode plots of (b) frequency dependent impedances and (c) frequency dependent phase angles.

https://doi.org/10.1371/journal.pone.0305611.g010

paper and went at anode surface, and/or might form a layer on the anode surface, which might be responsible for lower discharge capacity retention. This is also the indication of non-uniform mass transport mechanism in the coin cells [65]. Fig 10(B) shows the frequency dependent impedances of Bode plots. The plots remain at low resistances at high frequency, and show incline lines at low frequency, indicating energy storage capacitive behaviors of the prepared Mn_3O_4 nanoparticles. Fig 10(C) shows the frequency dependent phase angles of Bode plots. The highest phase angle is 20.33 to 34.21 degree for before and after BCD of 1000 cycles, show the pseudo capacitive behaviors of Zn^{2+} ion storage at low frequency region [66].

The specific discharge capacities with respect to applied current densities of different Mn-based materials are listed in Table 2. If one emphasize on the simplicity of preparation process and the cost of cathode plate fabrication, this study provides a simple and cost effective technique for a competitive cathode material production for ARZIBs.

Table 2. List of specific discharge capacities with respect to applied current densities of Mn-based cathodes in ARZIBs.

Cathode materials	Applied Current Density (mA/g)	Specific Discharge Capacity (mAh/g)	Reference
ε-MnO_2	0.1	221	[67]
Mn_3O_4	0.1	239	[17]
Mn_3O_4 nanodot	0.8	182	[68]
α-Mn_2O_3	0.2	137	[69]
Mn_3O_4@C	0.5	209	[19]
$MnCO_3$@ Mn_3O_4	0.2	165	[70]
Mn_2O_3/ Mn_3O_4 composite	1.0	122	[71]
Mn_3O_4@N dopped carbon coated carbon cloth	0.2	265	[72]
Mn_3O_4	1.0	87	[73]
Mn_3O_4@N dopped carbon matrix composite nanorods	0.1	280	[18]
$ZnMn_2O_4$	0.5	150	[74]
MnO_2/rGO/PANI	0.1	241	[75]
Core-shell Mn_3O_4/Carbon (Mn_3O_4@C) fiber	0.3	215	[76]
Mn_3O_4/GO composite	0.1	215	[77]
β-MnO_2	0.1	100	[78]
δ-MnO_2	0.1	126	[78]
α-MnO_2	0.02	210	[79]
α-MnO_2	0.05	255	[80]
α-MnO_2	0.06	302	[81]
α-MnO_2	0.09	290	[82]
δ-MnO_2	0.1	269	[83]
Mn_2O_3	0.1	150	[84]
Mn_3O_4	**0.1**	**240**	**This work**

https://doi.org/10.1371/journal.pone.0305611.t002

Conclusion

ARZIBs show auspicious candidate for secondary energy storage device by safety and environmental compatibility. However, poor cycle stability hinders its progresses. In this work, hausmannite Mn_3O_4 nanoparticles were synthesized by a thermal decomposition of Manganese (II) acetate tetrahydrate having rice powder as soft bio-template. Formation of Mn_3O_4 nanoparticles were confirmed by a series of spectroscopic and physico-chemical experiments. Fabricated CR-2032 coin cell of ARZIBs using prepared Mn_3O_4 nanoparticles as cathode material showed high specific discharge capacity with high columbic efficiency and excellent capacity retention after a long BCD cycling test. This work upholds the improvement of low cost ARZIBs.

Supporting information

S1 File. Supplementary figure.
(DOCX)

S1 Graphical abstract.
(TIF)

Author Contributions

Conceptualization: Nusrat Tazeen Tonu, Mohammad Abu Yousuf.

Formal analysis: Nusrat Tazeen Tonu.

Investigation: Nusrat Tazeen Tonu, Mohammad Abu Yousuf.

Methodology: Nusrat Tazeen Tonu, Parbhej Ahamed, Mohammad Abu Yousuf.

Software: Nusrat Tazeen Tonu, Parbhej Ahamed.

Supervision: Mohammad Abu Yousuf.

Validation: Mohammad Abu Yousuf.

Writing – original draft: Nusrat Tazeen Tonu.

Writing – review & editing: Nusrat Tazeen Tonu, Parbhej Ahamed, Mohammad Abu Yousuf.

References

1. Li C, Hu C, Song Y, Gao N, Yang W, Xu X. Microfluidic-oriented assembly of Mn_3O_4@ C/GFF cathode with multiscale synergistic structure for high-performance aqueous zinc-ion batteries. Carbon. 2023 May 1; 208:247–54. https://doi.org/10.1016/j.carbon.2023.03.058
2. Goodenough JB, Park KS. The Li-ion rechargeable battery: a perspective. Journal of the American Chemical Society. 2013 Jan 30; 135(4):1167–76. https://doi.org/10.1021/ja3091438 PMID: 23294028
3. Villa LC, Saldarriaga Agudelo W, Rojas NR. Estudio termodinámico de la lixiviación de plomo reciclado con citrato de sodio. Ciencia en Desarrollo. 2018 Dec; 9(2):119–26.
4. Tang B, Shan L, Liang S, Zhou J. Issues and opportunities facing aqueous zinc-ion batteries. Energy & Environmental Science. 2019; 12(11):3288–304. https://doi.org/10.1039/C9EE02526J
5. Wang N, Qiu X, Xu J, Huang J, Cao Y, Wang Y. Cathode materials challenge varied with different electrolytes in zinc batteries. ACS Materials Letters. 2021 Dec 20; 4(1):190–204. https://doi.org/10.1021/acsmaterialslett.1c00499
6. Jia X, Liu C, Neale ZG, Yang J, Cao G. Active materials for aqueous zinc ion batteries: synthesis, crystal structure, morphology, and electrochemistry. Chemical Reviews. 2020 Jul 27; 120(15):7795–866. https://doi.org/10.1021/acs.chemrev.9b00628 PMID: 32786670
7. Liu Y, Li Q, Ma K, Yang G, Wang C. Graphene oxide wrapped CuV2O6 nanobelts as high-capacity and long-life cathode materials of aqueous zinc-ion batteries. ACS nano. 2019 Sep 25; 13(10):12081–9. https://doi.org/10.1021/acsnano.9b06484 PMID: 31553172
8. Dai X, Wan F, Zhang L, Cao H, Niu Z. Freestanding graphene/VO_2 composite films for highly stable aqueous Zn-ion batteries with superior rate performance. Energy Storage Materials. 2019 Feb 1; 17:143–50. https://doi.org/10.1016/j.ensm.2018.07.022
9. Song TB, Huang ZH, Niu XQ, Zhang XR, Wei JS, Xiong HM. In-Situ Growth of Mn3O4 Nanoparticles on Nitrogen-Doped Carbon Dots-Derived Carbon Skeleton as Cathode Materials for Aqueous Zinc Ion Batteries. ChemSusChem. 2022 Mar 22; 15(6):e202102390. https://doi.org/10.1002/cssc.202102390 PMID: 35122400
10. Yin C, Chen J, Pan CL, Pan Y, Hu J. MOF-Derived Mn_3O_4@ C Hierarchical Nanospheres as Cathodes for Aqueous Zinc-Ion Batteries. ACS Applied Energy Materials. 2022 Nov 8; 5(11):14144–54. https://doi.org/10.1021/acsaem.2c02690
11. Selvakumaran D, Pan A, Liang S, Cao G. A review on recent developments and challenges of cathode materials for rechargeable aqueous Zn-ion batteries. Journal of Materials Chemistry A. 2019; 7 (31):18209–36. https://doi.org/10.1039/C9TA05053A
12. Liao Y, Chen HC, Yang C, Liu R, Peng Z, Cao H, et al. Unveiling performance evolution mechanisms of MnO_2 polymorphs for durable aqueous zinc-ion batteries. Energy Storage Materials. 2022 Jan 1; 44:508–16. https://doi.org/10.1016/j.ensm.2021.10.039
13. Siamionau U, Aniskevich Y, Mazanik A, Kokits O, Ragoisha G, Jo JH, et al. Rechargeable zinc-ion batteries with manganese dioxide cathode: How critical is choice of manganese dioxide polymorphs in aqueous solutions?. Journal of Power Sources. 2022 Mar 1; 523:231023. https://doi.org/10.1016/j.jpowsour.2022.231023
14. Liu S, Li MY, Zhang J, Su D, Huang Z, Kunwar S, et al. Self-assembled Al nanostructure/ZnO quantum dot heterostructures for high responsivity and fast UV photodetector. Nano-micro letters. 2020 Dec; 12:1–3. https://doi.org/10.1007/s40820-020-00455-9 PMID: 34138130
15. Zhu SY, Yuan YF, Du PF, Mo CL, Cai GC, Wang BX, et al. Ultrasmall Mn_3O_4 nanocrystalline@ three-dimensional macroporous honeycomb-like hollow carbon matrix for high-rate and long-lifetime zinc-ion storage. Electrochimica Acta. 2022 Jul 1; 419:140396. https://doi.org/10.1016/j.electacta.2022.140396

16. Guo Y, Zhang Y, Lu H. Manganese-based materials as cathode for rechargeable aqueous zinc-ion batteries. Battery Energy. 2022 Apr; 1(2):20210014. https://doi.org/10.1002/bte2.20210014

17. Hao J, Mou J, Zhang J, Dong L, Liu W, Xu C, et al. Electrochemically induced spinel-layered phase transition of Mn_3O_4 in high performance neutral aqueous rechargeable zinc battery. Electrochimica Acta. 2018 Jan 1; 259:170–8. https://doi.org/10.1016/j.electacta.2017.10.166

18. Sun M, Li DS, Wang YF, Liu WL, Ren MM, Kong FG, et al. Mn_3O_4@ NC composite nanorods as a cathode for rechargeable aqueous Zn-ion batteries. ChemElectroChem. 2019 May 2; 6(9):2510–6. https://doi.org/10.1002/celc.201900376

19. Chen H, Zhou W, Zhu D, Liu Z, Feng Z, Li J, et al. Porous cube-like Mn_3O_4@ C as an advanced cathode for low-cost neutral zinc-ion battery. Journal of Alloys and Compounds. 2020 Jan 15; 813:151812. https://doi.org/10.1016/j.jallcom.2019.151812

20. Zhang H, Liu D, Wei Y, Li A, Liu B, Yuan Y, et al. Fabrication of a 1D Mn_3O_4 nano-rod electrode for aqueous asymmetric supercapacitors and capacitive deionization. Inorganic Chemistry Frontiers. 2019; 6(2):355–65. https://doi.org/10.1039/C8QI00993G

21. Liu Z, Zhang L, Xu G, Zhang L, Jia D, Zhang C. Mn_3O_4 hollow microcubes and solid nanospheres derived from a metal formate framework for electrochemical capacitor applications. RSC advances. 2017; 7(18):11129–34. https://doi.org/10.1039/C7RA00435D

22. Liu H, Xue Q, Zhao J, Zhang Q. Enhanced supercapacitive performance of binary cooperative complementary $Co(OH)_2/Mn_3O_4$ nanomaterials directly synthesized through ion diffusion method controlled by ion exchange membrane. Electrochimica Acta. 2018 Jan 10; 260:330–7. https://doi.org/10.1016/j.electacta.2017.12.067

23. Yang D, Fan T, Zhou H, Ding J, Zhang D. Biogenic hierarchical TiO_2/SiO_2 derived from rice husk and enhanced photocatalytic properties for dye degradation. PLoS One. 2011 Sep 9; 6(9):e24788. https://doi.org/10.1371/journal.pone.0024788

24. Visinescu D, Patrinoiu G, Tirsoaga A, Carp O. Polysaccharides route: a new green strategy for metal oxides synthesis. Environmental Chemistry for a Sustainable World: Volume 1: Nanotechnology and Health Risk. 2012:119–69. https://doi.org/10.1007/978-94-007-2442-6_5

25. Rahman MM, Hasnida N, Nik WW. Preparation of zeolite Y using local raw material rice husk as a silica source. Journal of Scientific Research. 2009 Apr 22; 1(2):285–91. https://doi.org/10.3329/jsr.v1i2.1777

26. Zhang G, Shen X, Yang Y. Facile synthesis of monodisperse porous ZnO spheres by a soluble starch-assisted method and their photocatalytic activity. The Journal of Physical Chemistry C. 2011 Apr 21; 115(15):7145–52. https://doi.org/10.1021/jp110256s

27. Taubert A, Wegner G. Formation of uniform and monodisperse zincite crystals in the presence of soluble starch. Journal of Materials Chemistry. 2002; 12(4):805–7. https://doi.org/10.1039/B110424C

28. Ulfa M, Prasetyoko D, Bahruji H, Nugraha RE. Green synthesis of hexagonal hematite (α-Fe2O3) flakes using pluronic F127-gelatin template for adsorption and photodegradation of ibuprofen. Materials. 2021 Nov 10; 14(22):6779. https://doi.org/10.3390/ma14226779

29. Hosny NM, Dahshan A. Facile synthesis and optical band gap calculation of Mn_3O_4 nanoparticles. Materials Chemistry and Physics. 2012 Dec 14; 137(2):637–43. https://doi.org/10.1016/j.matchemphys.2012.09.068

30. Hoang Huy VP, Hieu LT, Hur J. Zn metal anodes for Zn-ion batteries in mild aqueous electrolytes: Challenges and strategies. Nanomaterials. 2021 Oct 17; 11(10):2746. https://doi.org/10.3390/nano11102746 PMID: 34685186

31. Wang Y, Hou C, Lin X, Jiang H, Zhang C, Liu G. Dye degradation studies of hausmannite manganese oxide (Mn_3O_4) nanoparticles synthesized by chemical method. Applied Physics A. 2021 Apr; 127:1–7. https://doi.org/10.1007/s00339-021-04428-6

32. Atique Ullah AK, Fazle Kibria AK, Akter M, Khan MN, Tareq AR, Firoz SH. Oxidative degradation of methylene blue using Mn_3O_4 nanoparticles. Water Conservation Science and Engineering. 2017 Mar; 1:249–56. https://doi.org/10.1007/s41101-017-0017-3

33. Vázquez-Olmos A, Redón R, Rodríguez-Gattorno G, Mata-Zamora ME, Morales-Leal F, Fernández-Osorio AL, et al. One-step synthesis of Mn3O4 nanoparticles: Structural and magnetic study. Journal of colloid and interface science. 2005 Nov 1; 291(1):175–80. https://doi.org/10.1016/j.jcis.2005.05.005 PMID: 16005011

34. Ito VC, Bet CD, Wojeicchowski JP, Demiate IM, Spoto MH, Schnitzler E, et al. Effects of gamma radiation on the thermoanalytical, structural and pasting properties of black rice (Oryza sativa L.) flour. Journal of Thermal Analysis and Calorimetry. 2018 Jul; 133:529–37. https://doi.org/10.1007/s10973-017-6766-6

35. Ghaedi H, Zhao M. Review on template removal techniques for synthesis of mesoporous silica materials. Energy & Fuels. 2022 Feb 19; 36(5):2424–46. https://doi.org/10.1021/acs.energyfuels.1c04435

36. Rajalakshmi R, Remya KP, Viswanathan C, Ponpandian N. Enhanced electrochemical activities of morphologically tuned $MnFe_2O_4$ nanoneedles and nanoparticles integrated on reduced graphene oxide for highly efficient supercapacitor electrodes. Nanoscale Advances. 2021; 3(10):2887–901. https://doi.org/10.1039/D1NA00144B

37. Mahajan H, Kumar S, Sharma A, Mohammed I, Thakur M, Kaur A, et al. Effect of sintering temperature on structural, morphological, magnetic, and electrochemical properties of $Mn_{0.3}Co_{0.2}Zn_{0.5}Fe_2O_4$ Ferrite. Journal of Sol-Gel Science and Technology. 2023 Feb; 105(2):388–404. https://doi.org/10.1007/s10971-022-06022-5

38. Satomi KI. Oxygen positional parameters of tetragonal Mn_3O_4. Journal of the Physical Society of Japan. 1961 Feb; 16(2):258–66. https://doi.org/10.1143/JPSJ.16.258

39. Jamil S, Khan SR, Sultana B, Hashmi M, Haroon M, Janjua MR. Synthesis of saucer shaped manganese oxide nanoparticles by co-precipitation method and the application as fuel additive. Journal of Cluster Science. 2018 Nov; 29:1099–106. https://doi.org/10.1007/s10876-018-1428-9

40. Monshi A, Foroughi MR, Monshi MR. Modified Scherrer equation to estimate more accurately nanocrystallite size using XRD. World journal of nano science and engineering. 2012 Sep 28; 2(3):154–60.

41. Rizky A, Fadhillah A. Python-based Program for Analysing Lattice Parameter of Cubic and Tetragonal Crystal Structure. InJournal of Physics: Conference Series 2021 Oct 1 (Vol. 2019, No. 1, p. 012070). IOP Publishing. https://doi.org/10.1088/1742-6596/2019/1/012070

42. Tholkappiyan R, Naveen AN, Vishista K, Hamed F. Investigation on the electrochemical performance of hausmannite Mn_3O_4 nanoparticles by ultrasonic irradiation assisted co-precipitation method for supercapacitor electrodes. Journal of Taibah University for Science. 2018 Sep 3; 12(5):669–77. https://doi.org/10.1080/16583655.2018.1497440

43. Shah HU, Wang F, Toufiq AM, Ali S, Khan ZU, Li Y, et al. Electrochemical properties of controlled size Mn_3O_4 nanoparticles for supercapacitor applications. Journal of nanoscience and nanotechnology. 2018 Jan 1; 18(1):719–24. https://doi.org/10.1166/jnn.2018.14644

44. Mahamad Yusoff NF, Idris NH, Md Din MF, Majid SR, Harun NA, Rahman MM. Electrochemical sodiation/desodiation into Mn_3O_4 nanoparticles. ACS omega. 2020 Nov 3; 5(45):29158–67. https://doi.org/10.1021/acsomega.0c03888

45. Naderi M. Surface area: brunauer–emmett–teller (BET). InProgress in filtration and separation 2015 Jan 1 (pp. 585–608). Academic Press. https://doi.org/10.1016/B978-0-12-384746-1.00014-8

46. Thalji MR, Ali GA, Liu P, Zhong YL, Chong KF. $W_{18}O_{49}$ nanowires-graphene nanocomposite for asymmetric supercapacitors employing $AlCl_3$ aqueous electrolyte. Chemical Engineering Journal. 2021 Apr 1; 409:128216. https://doi.org/10.1016/j.cej.2020.128216

47. Zhang Y, Yang Y, Zhang Y, Zhang T, Ye M. Heterogeneous oxidation of naproxen in the presence of α-MnO_2 nanostructures with different morphologies. Applied Catalysis B: Environmental. 2012 Oct 30; 127:182–9. 10.1016/j.apcatb.2012.08.014

48. Thalji MR, Ali GA, Shim JJ, Chong KF. Cobalt-doped tungsten suboxides for supercapacitor applications. Chemical Engineering Journal. 2023 Oct 1; 473:145341. https://doi.org/10.1016/j.cej.2023.145341

49. Hanifehpour Y, Joo SW, Hamnabard N, Jung JH. The electrochemical performance and catalytic properties of Ytterbium substitution on Manganese oxide nanoparticles: BET study; preparation and characterization. Journal of Materials Science: Materials in Electronics. 2019 Oct; 30:18897–909. https://doi.org/10.1007/s10854-019-02246-4

50. Zhong M, Jang M. Light absorption coefficient measurement of SOA using a UV–Visible spectrometer connected with an integrating sphere. Atmospheric environment. 2011 Aug 1; 45(25):4263–71. 10.1016/j.atmosenv.2011.04.082

51. López R, Gómez R. Band-gap energy estimation from diffuse reflectance measurements on sol–gel and commercial TiO_2: a comparative study. Journal of sol-gel science and technology. 2012 Jan; 61:1–7. https://doi.org/10.1007/s10971-011-2582-9

52. Fritzsche H. The origin of reversible and irreversible photostructural changes in chalcogenide glasses. Philosophical Magazine B. 1993 Oct 1; 68(4):561–72. https://doi.org/10.1080/13642819308217935

53. Dubal DP, Dhawale DS, Salunkhe RR, Pawar SM, Lokhande CD. A novel chemical synthesis and characterization of Mn_3O_4 thin films for supercapacitor application. Applied Surface Science. 2010 May 1; 256(14):4411–6. https://doi.org/10.1016/j.apsusc.2009.12.057

54. Zhu C, Fang G, Zhou J, Guo J, Wang Z, Wang C, et al. Binder-free stainless steel@ Mn_3O_4 nanoflower composite: a high-activity aqueous zinc-ion battery cathode with high-capacity and long-cycle-life. Journal of Materials Chemistry A. 2018; 6(20):9677–83. https://doi.org/10.1039/C8TA01198B

55. Liu X, Cui L, Yu K, Lv J, Liu Y, Ma Y, et al. Cu/Ag complex modified Keggin-type coordination polymers for improved electrochemical capacitance, dual-function electrocatalysis, and sensing performance.

Inorganic Chemistry. 2021 Aug 30; 60(18):14072–82. https://doi.org/10.1021/acs.inorgchem.1c01397 PMID: 34455794

56. Lan K, Wei Q, Wang R, Xia Y, Tan S, Wang Y, et al. Two-dimensional mesoporous heterostructure delivering superior pseudocapacitive sodium storage via bottom-up monomicelle assembly. Journal of the American Chemical Society. 2019 Sep 30; 141(42):16755–62. https://doi.org/10.1021/jacs.9b06962 PMID: 31564098

57. Muller GA, Cook JB, Kim HS, Tolbert SH, Dunn B. High performance pseudocapacitor based on 2D layered metal chalcogenide nanocrystals. Nano letters. 2015 Mar 11; 15(3):1911–7. https://doi.org/10.1021/nl504764m PMID: 25654445

58. Chen C, Wen Y, Hu X, Ji X, Yan M, Mai L, et al. Na^+ intercalation pseudocapacitance in graphene-coupled titanium oxide enabling ultra-fast sodium storage and long-term cycling. Nature communications. 2015 Apr 24; 6(1):6929. https://doi.org/10.1038/ncomms7929

59. Chao D, Liang P, Chen Z, Bai L, Shen H, Liu X, et al. Pseudocapacitive Na-ion storage boosts high rate and areal capacity of self-branched 2D layered metal chalcogenide nanoarrays. ACS nano. 2016 Nov 22; 10(11):10211–9. https://doi.org/10.1021/acsnano.6b05566 PMID: 27768284

60. Ye Z, Li P, Wei W, Huang C, Mi L, Zhang J, et al. In Situ Anchoring Anion-Rich and Multi-Cavity NiS_2 Nanoparticles on NCNTs for Advanced Magnesium-Ion Batteries. Advanced Science. 2022 Jun; 9(18):2200067. https://doi.org/10.1002/advs.202200067

61. Huang C, Wang Q, Tian G, Zhang D. Oxygen vacancies-enriched Mn_3O_4 enabling high-performance rechargeable aqueous zinc-ion battery. Materials Today Physics. 2021 Nov 1; 21:100518. https://doi.org/10.1016/j.mtphys.2021.100518

62. Bai Y, Qin Y, Hao J, Zhang H, Li CM. Advances and Perspectives of Ion-Intercalated Vanadium Oxide Cathodes for High-Performance Aqueous Zinc Ion Battery. Advanced Functional Materials. 2024 Mar; 34(11):2310393. https://doi.org/10.1002/adfm.202310393

63. Lakshmi D, Nalini B. Performance of SnSb: Ce, Co alloy as anode for lithium-ion batteries. Journal of Solid State Electrochemistry. 2017 Apr; 21:1027–34. https://doi.org/10.1007/s10008-016-3456-4

64. Palaniyandy N, Lakshmi D, Thenmozhi G, Kheawhom S, Musyoka NN. Enhanced electrochemical energy storage devices utilizing a one-dimensional (1D) α-MnO_2 nanocomposite encased in onion-like carbon. Journal of Materials Science. 2024 Mar 27:1–20. https://doi.org/10.1007/s10853-024-09373-2

65. Aboelazm EA, Ali GA, Algarni H, Yin H, Zhong YL, Chong KF. Magnetic electrodeposition of the hierarchical cobalt oxide nanostructure from spent lithium-ion batteries: its application as a supercapacitor electrode. The Journal of Physical Chemistry C. 2018 May 21; 122(23):12200–6. https://doi.org/10.1021/acs.jpcc.8b03306

66. Ibukun O, Jeong HK. An activated carbon and carbon nanotube composite for a high-performance capacitor. New Phys. Sae. Mulli. 2018 Feb 28; 68:185–8. 10.3938/NPSM.68.185

67. Wang L, Cao X, Xu L, Chen J, Zheng J. Transformed akhtenskite MnO_2 from Mn_3O_4 as cathode for a rechargeable aqueous zinc ion battery. ACS sustainable chemistry & engineering. 2018 Oct 30; 6(12):16055–63. 10.1021/acssuschemeng.8b02502

68. Jiang L., Wu Z., Wang Y., Tian W., Yi Z., Cai C., et al., 2019. Ultrafast zinc-ion diffusion ability observed in 6.0-nanometer spinel nanodots. *ACS nano*, 13(9), pp.10376–10385. https://doi.org/10.1021/acsnano.9b04165 PMID: 31381305

69. Jiang B., Xu C., Wu C., Dong L., Li J., & Kang F. (2017). Manganese sesquioxide as cathode material for multivalent zinc ion battery with high capacity and long cycle life. *Electrochimica Acta*, 229, 422–428. https://doi.org/10.1016/j.electacta.2017.01.163

70. Li T, Tong J, Liu S, Liang J, Dai G, Sun W, et al. Butterfly-tie like $MnCO_3$@ Mn_3O_4 heterostructure enhanced the electrochemical performances of aqueous zinc ion batteries. Journal of Colloid and Interface Science. 2024 Feb 15; 656:504–12. https://doi.org/10.1016/j.jcis.2023.11.129

71. Yao J, Liu Y, Li Y, Jiang J, Zhu Q. Facile synthesis of Mn2O3/Mn3O4 composites with superior zinc ion storage performance. Materials Research Bulletin. 2023 Sep 1; 165:112292. https://doi.org/10.1016/j.materresbull.2023.112292

72. Zhou Z, Liu S, Wang J, Wu Y, Yang Y, Li Y, et al. Enhanced cycling stability achieved by the nitrogen doped carbon coating layer for electrodeposited Mn3O4 in aqueous zinc ion batteries. Applied Surface Science. 2023 Mar 30; 614:156259. https://doi.org/10.1016/j.apsusc.2022.156259

73. Gong L, Zhang Y, Li Z. Construction of novel hierarchical honeycomb-like Mn_3O_4 MnO_2 core-shell architecture with high voltage for advanced aqueous zinc-ion batteries. Journal of The Electrochemical Society. 2022 Apr 11; 169(4):040519. https://doi.org/10.1149/1945-7111/ac638d

74. Zhang N, Cheng F, Liu Y, Zhao Q, Lei K, Chen C, et al. Cation-deficient spinel ZnMn2O4 cathode in Zn (CF3SO3) 2 electrolyte for rechargeable aqueous Zn-ion battery. Journal of the American Chemical Society. 2016 Oct 5; 138(39):12894–901. https://doi.org/10.1021/jacs.6b05958 PMID: 27627103

75. Mao J, Wu FF, Shi WH, Liu WX, Xu XL, Cai GF, et al. Preparation of polyaniline-coated composite aerogel of MnO_2 and reduced graphene oxide for high-performance Zinc-ion battery. Chinese Journal of Polymer Science. 2020 May; 38:514–21. https://doi.org/10.1007/s10118-020-2353-6

76. Long J, Yang Z, Yang F, Cuan J, Wu J. Electrospun core-shell Mn_3O_4/carbon fibers as high-performance cathode materials for aqueous zinc-ion batteries. Electrochimica Acta. 2020 Jun 1; 344:136155. https://doi.org/10.1016/j.electacta.2020.136155

77. Huang Z, Duan Y, Jing Q, Sun M, Tang B, Shi S. Assembly of Mn_3O_4 nanoparticles at low temperature on graphene with enhanced electrochemical property for zinc-ion battery. Journal of Alloys and Compounds. 2021 May 25; 864:158316. https://doi.org/10.1016/j.jallcom.2020.158316

78. Guo C, Zhou Q, Liu H, Tian S, Chen B, Zhao J, et al. A case study of β-and δ-MnO_2 with different crystallographic forms on ion-storage in rechargeable aqueous zinc ion battery. Electrochimica Acta. 2019 Nov 20; 324:134867. https://doi.org/10.1016/j.electacta.2019.134867

79. Lee B, Yoon CS, Lee HR, Chung KY, Cho BW, Oh SH. Electrochemically-induced reversible transition from the tunneled to layered polymorphs of manganese dioxide. Scientific reports. 2014 Aug 14; 4 (1):6066. https://doi.org/10.1038/srep06066 PMID: 25317571

80. Lee J, Ju JB, Cho WI, Cho BW, Oh SH. Todorokite-type MnO_2 as a zinc-ion intercalating material. Electrochimica Acta. 2013 Dec 1; 112:138–43. https://doi.org/10.1016/j.electacta.2013.08.136

81. Li H, Liu Z, Liang G, Huang Y, Huang Y, Zhu M, et al. Waterproof and tailorable elastic rechargeable yarn zinc ion batteries by a cross-linked polyacrylamide electrolyte. ACS nano. 2018 Mar 28; 12 (4):3140–8. https://doi.org/10.1021/acsnano.7b09003 PMID: 29589438

82. Sun W, Wang F, Hou S, Yang C, Fan X, Ma Z, et al. Zn/MnO2 battery chemistry with H^+ and Zn^{2+} coinsertion. Journal of the American Chemical Society. 2017 Jul 26; 139(29):9775–8. https://doi.org/10.1021/jacs.7b04471

83. Wei C, Xu C, Li B, Du H, Kang F. Preparation and characterization of manganese dioxides with nanosized tunnel structures for zinc ion storage. Journal of Physics and Chemistry of Solids. 2012 Dec 1; 73 (12):1487–91. https://doi.org/10.1016/j.jpcs.2011.11.038

84. Jiang B, Xu C, Wu C, Dong L, Li J, Kang F. Manganese sesquioxide as cathode material for multivalent zinc ion battery with high capacity and long cycle life. Electrochimica Acta. 2017 Mar 1; 229:422–8. https://doi.org/10.1016/j.electacta.2017.01.163